RECENT RESULTS FROM CDF

The CDF Collaboration[1,2]

Presented by James F. Patrick

Fermi National Accelerator Laboratory

Batavia IL 60510

USA

ABSTRACT

Recent results in the areas of b quark production, electroweak measurements, new particle searches, and QCD tests from the study of $\bar{p}p$ collisions at a center of mass energy of 1.8 TeV from the CDF detector are presented.

1 Introduction

Presented are recent results from the CDF experiment, which studies $\bar{p}p$ collisions at the Fermilab Tevatron. The data sample used corresponds to approximately 4.5 pb^{-1} at a center of mass energy of 1.8 TeV, accumulated during the 1988-89 data-taking run.

The detector has been extensively described elsewhere [1], only a brief description is included here. Figure 1 shows a side view of the detector. It contains calorimeters covering the pseudorapidity range $-4.2 \leq \eta \leq 4.2$ and the entire azimuthal range constructed in a projective tower geometry. Lead and steel plates are used as the absorbing medium in the electromagnetic and hadronic sections respectively. The calorimetry is divided into central ($|\eta| \leq 1.1$), endplug ($1.1 \leq |\eta| \leq 2.2$) and forward ($2.2 \leq |\eta| \leq 4.2$) sections. The central section uses plastic scintillator as the sampling medium, here the tower segmentation is 0.1 units in $\Delta\eta$ and 15° in $\Delta\phi$. In the endplug and forward sections, proportional chambers are used as the sampling medium, where the segmentation is 0.1 units in $\Delta\eta$ and 5° in $\Delta\phi$. Proportional chambers with cathode strip readout ("strip chambers") are embedded in the central and plug electromagnetic calorimeters. These provide precise position information for electron and photon showers.

The event vertex is is determined by a set of 8 time projection chambers surrounding the beam pipe. Charged tracks in the region $|\eta| < 1$ are reconstructed in an 88 layer drift chamber immersed in a 1.4 Tesla magnetic field. The momentum

[1] Argonne - Brandeis - Chicago - Duke - Fermilab - Frascati - Harvard- Illinois - Johns Hopkins - KEK - LBL - Michigan - MIT - New Mexico - Osaka City - Padova - Pennsylvania - Pisa - Pittsburg - Purdue - Rochester - Rockefeller - Rutgers - SSCL - Texas A&M- Tsukuba - Tufts - UCLA - Wisconsin - Yale

[2] Supported by the U.S. Department of Energy, contract number DE-AC02-76CH03000.

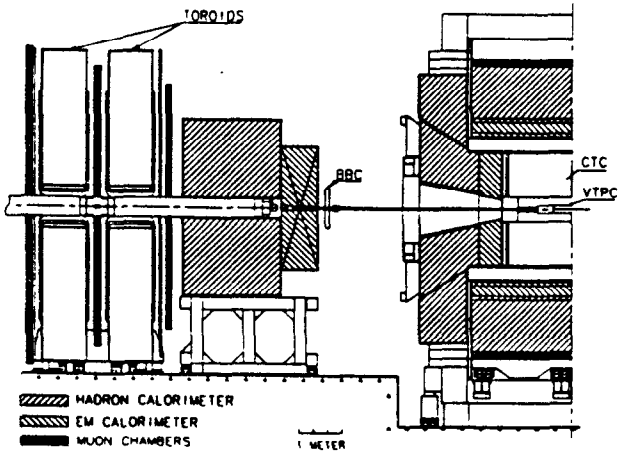

Figure 1: Side view of the CDF detector. Only one half of the detector is shown.

resolution is $\sigma_{pt}/p_t = 0.2\% \times p_t$ in general and $0.11\% \times p_t$ for tracks constrained to the event vertex.

Recent results are presented on inclusive b quark production including reconstruction of exclusive decays of B mesons. W and Z cross sections and a test of lepton universality in W decays are also presented. Searches for new massive vector bosons, the top quark, supersymmetry, and heavy stable particles are described. Tests of QCD including comparisons with recent Next to Leading Order calculations are discussed. Also presented are studies of direct photon production including the photon angular distribution and two photon production. Finally, a new measurement of the total cross section is presented.

2 B Quark Production

2.1 Inclusive b-quark Production

B quarks are produced very copiously at the Tevatron Collider. Next to Leading Order ($\mathcal{O}\ \alpha^3$) calculations of the production cross section have been performed by Nason, Dawson, and Ellis [2]. Although the cross section is largest in the forward direction and at low p_t, for b quarks produced with rapidity ($y < 1$) and $p_t > 10$ GeV, the cross section is estimated to be a fairly large 1.5 μb. For the recent collider run where 4.5 pb^{-1} was collected this corresponds to 6.75 million produced b's! A measurement of this cross section provides an important check of the QCD calculation. It is also an important measurement for determining the feasibility of experiments at hadron colliders to measure weak decay parameters and search for CP violation in the b system.

The b cross section is measured by CDF primarily from a study of inclusive electron production [3]. Starting with events with candidate electrons, W and Z events are removed by missing E_t and e^+e^- mass cuts. Low mass pairs consistent with conversions are also removed. The charm contribution is estimated using the ISAJET [4] Monte Carlo and subtracted. Figure 2 shows the inclusive electron distribution compared to the ISAJET predictions. The agreement is seen to be very good.

The b production cross section as a function of p_t is inferred from this distribution using ISAJET. ISAJET is adjusted to reproduce the theoretical b p_t distribution and the Peterson [5] distribution for b quark fragmentation. Measured B decay branching ratios are used where available. The electron identification efficiency is determined from test beam and collider data. The result is shown in Fig. 3 together with the theoretical prediction of Nason, Dawson and Ellis. Note the cross sections displayed are the integrated value above some p_{tmin}. The dashed lines indicate the theoretical uncertainties. The measured cross sections appear systematically above the theory. There is some expectation that large higher order contributions in the lower x region probed by CDF might explain the result [6, 7, 8].

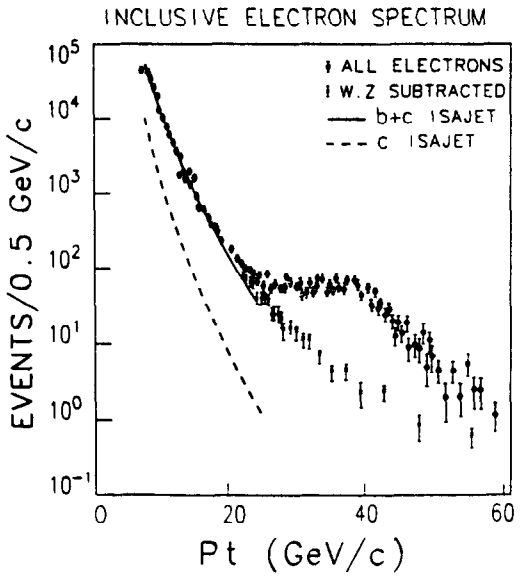

Figure 2: The inclusive electron p_t distribution compared to predictions of the ISAJET Monte Carlo normalized to the data.

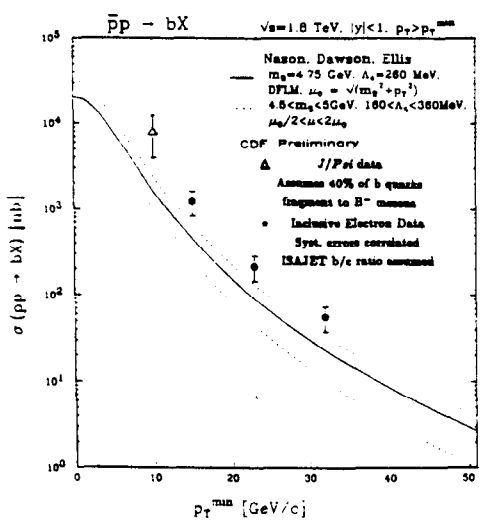

Figure 3: The inclusive b cross section, plotted as an integral above a fixed value of p_{tmin}. Also shown are the predictions of Nason, Dawson and Ellis [2].

2.2 Associated Charm Production

Several checks have been performed to demonstrate that the charm contribution to the inclusive electron distribution is in fact small. A search was performed for D^0 mesons in a cone of size $R_{\eta-\phi} < 1.0$ in $\eta - \phi$ space about the electron. If the electrons were due to charm pair production, then one would expect $e^- - \overline{D^0}$ (and the charge conjugate). However for b production, $e^- - D^0$ + the charge conjugate should predominate. Figure 4 shows the observed D^0 signal; it has the configuration expected for b production. Similarly, a K^{*0} signal is seen in conjunction with e^- consistent with b production (Fig. 4). If charm pair production were the source of the electrons, then one would expect roughly equal numbers of $e^- - \overline{K^{*0}}$ and $e^- - K^{*0}$ combinations.

2.3 Exclusive B Decays

Until recently, reconstruction of exclusive B meson decays has only been accomplished by e^+e^- experiments with center of mass energies in the upsilon region. Despite the much greater event complexity, the CDF experiment is able to take advantage of the large number of produced b's combined with the significant b decay branching fraction to J/ψ to reconstruct exclusive B meson decays. J/ψ's are cleanly identified in the detector via their decay to $\mu^+\mu^-$. Candidate J/ψ's within 50 MeV of the nominal mass are selected and constrained to the nominal mass (Fig. 5a). Mass combinations of the J/ψ with tracks within a 60^0 cone are formed. Signals are observed for the modes $B^\pm \rightarrow J/\psi K^\pm$ (Fig. 5b) and $B^0, \overline{B}^0 \rightarrow J/\psi K^{*0}, \overline{K}^{*0}$ (Fig. 5c). The combined signals are shown in Fig. 5d. A fit to this distribution gives a mass of 5.279±0.006 GeV.

This signal provides another measurement of the b production cross section. Only the $J/\psi - K^\pm$ mode is included here. ISAJET is again used to determine the detection efficiency; this turns out to be 0.5%. Using the measured branching fraction for this decay gives a cross section for b production with $p_t > 10.5$ GeV and $|y| < 1$ of $8.5 \pm 2.1(stat.) \pm 3.8(sys.)\mu$b. This point is displayed in Fig. 3 together with the measurements based on inclusive electron production. It follows the trend of those measurements, lying above the theoretical predictions.

2.4 χ Production

Observed J/ψ's are expected to be predominantly from decays of directly produced χ states and from decays of B mesons. Direct J/ψ production is suppressed in hadronic collisions as it must occur via a three gluon vertex [9]. Measurements of χ production together with inclusive J/ψ production could provide an additional handle on the b production cross section. However this picture is somewhat complicated by the recent observation of the decay $B \rightarrow \chi + X$ by the Argus collaboration [10].

J/ψ candidates with $p_t > 6$ GeV are selected. Calorimeter towers with $E_t > 1$ GeV are combined with the J/ψ and the mass difference M($J/\psi - \gamma$) - M(J/ψ)

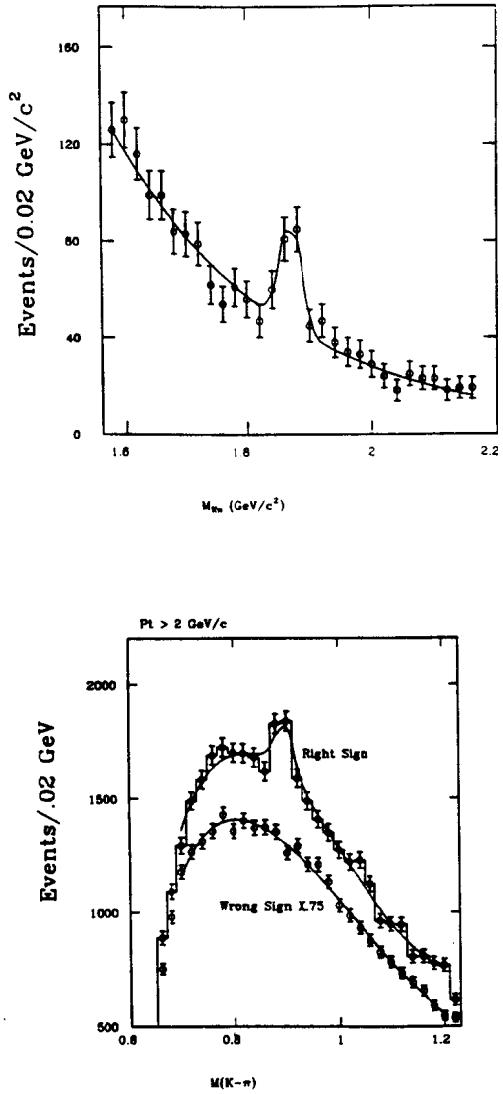

Figure 4: Signal for D^0 for same sign combinations of e and K in the inclusive electron sample. No signal in the opposite sign combination is observed. Also shown is the K^{*0} peak associated with same sign $e-K$ combinations, again no significant signal is seen in the opposite sign combination.

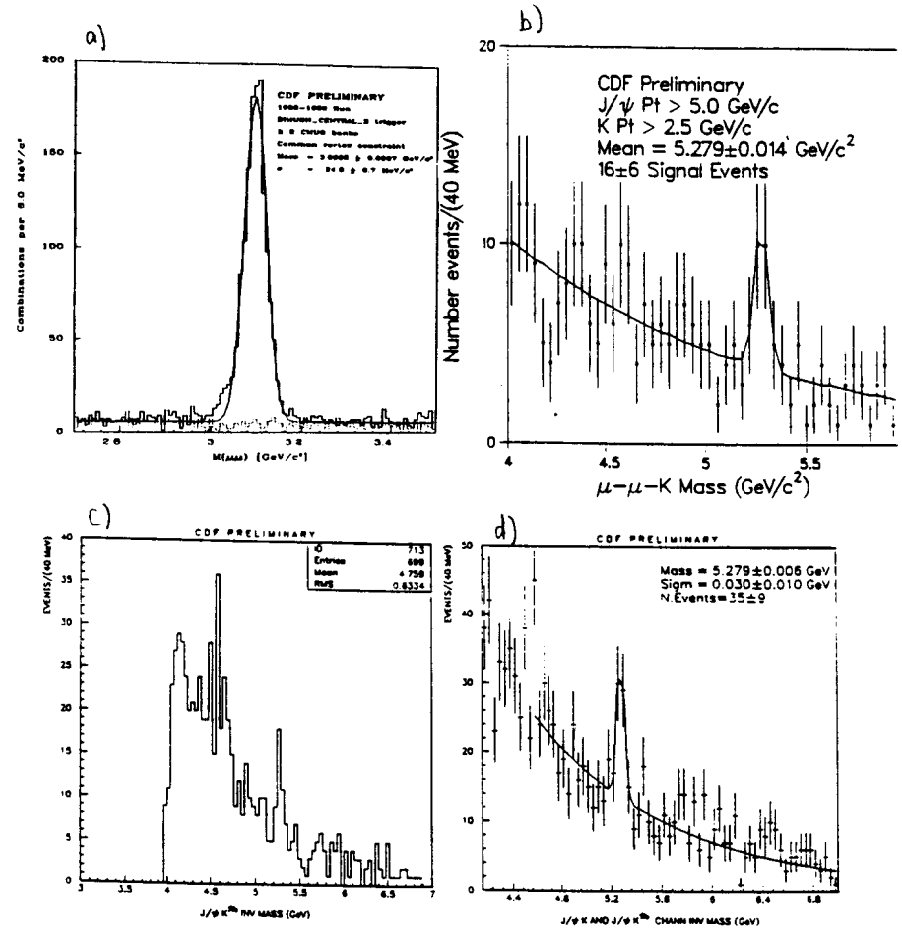

Figure 5: a) Invariant mass of $\mu^+\mu^-$ pairs in the J/ψ region. b) Invariant mass of $J/\psi - K^{\pm}$ combinations. c) Invariant mass of $J/\psi - K^{*0}$ combinations. d) Combined b) and c).

formed. The photon direction is determined using the position in the strip chambers. Figure 6 shows this mass difference; a clear signal is seen at $\Delta M = 412 \pm 15$ MeV. This is consistent with the expected peak at 424 MeV, assuming 60% of the J/ψ's are from χ_1 and the remainder from χ_2. A fit to the distribution using a Gaussian plus polynomial background yields 75.3 ± 12.0 detected χ's.

The geometrical acceptance is computed using ISAJET modified to include direct χ production (ISACHI). The efficiency for the photon is determined using GEANT. The GEANT calculation is verified by studying the efficiency for detecting the low energy electron in asymmetric photon conversion pairs. Finally, it is determined that $37.4 \pm 6.8(stat.) \pm 26(sys.)\%$ of the J/ψ's come from χ's. However the process $B \rightarrow \chi + X$ must be better understood before infering a b production cross section from this measurement.

2.5 $B^0 - \overline{B}^0$ Mixing

$B^0 - \overline{B^0}$ mixing occurs through the box diagrams show in Fig. 7. Measurements of this process give information on the CKM matrix elements $|V_{td}|^2$ and $|V_{ts}|^2$. $B_s^0 - \overline{B_s^0}$ mixing is expected to be much larger than $B_d^0 - \overline{B_d^0}$ as the far off diagonal CKM matrix elements are small.

Mixing is described by the parameter χ

$$\chi_{d,s} = \frac{N(B_{d,s}^0 \rightarrow \overline{B}_{d,s}^0)}{N(B_{d,s}^0 \rightarrow B_{d,s}^0) + N(\overline{B}_{d,s}^0 \rightarrow \overline{B}_{d,s}^0)} \quad . \tag{1}$$

Experimentally, what is measured is the ratio of like to unlike sign lepton pairs R

$$R = \frac{N(l^+l^+ + l^-l^-)}{N(l^+l^- + l^-l^+)} \tag{2}$$

from leptonic decays of b pairs. R is related to χ by the relation

$$R = \frac{2\chi(1-\chi) + [(1-\chi)^2 + \chi^2]f_s}{[(1-\chi)^2 + \chi^2] + 2\chi(1-\chi)f_s + f_c} \tag{3}$$

where f_c is the fraction of like sign pairs from charm and f_s is the fraction of like sign pairs from the non-mixing process $B \rightarrow l; \overline{B} \rightarrow \overline{D} \rightarrow l$. Whereas B_s and B_d are not distinguishable, the measured value is actually

$$\chi = P_d\chi_d + P_s\chi_s \tag{4}$$

where P_d and P_s are the relative fractions of B_d and B_s respectively.

Both $e - \mu$ and $e - e$ events are used in the measurement [13]. $e - \mu$ events have the advantage that they lack backgrounds from Drell-Yan and vector meson production. To reduce background from sequential B decay ($B \rightarrow Dl \rightarrow Dll$) the dilepton mass is required to exceed 5 GeV. For di-electron events, the upsilon

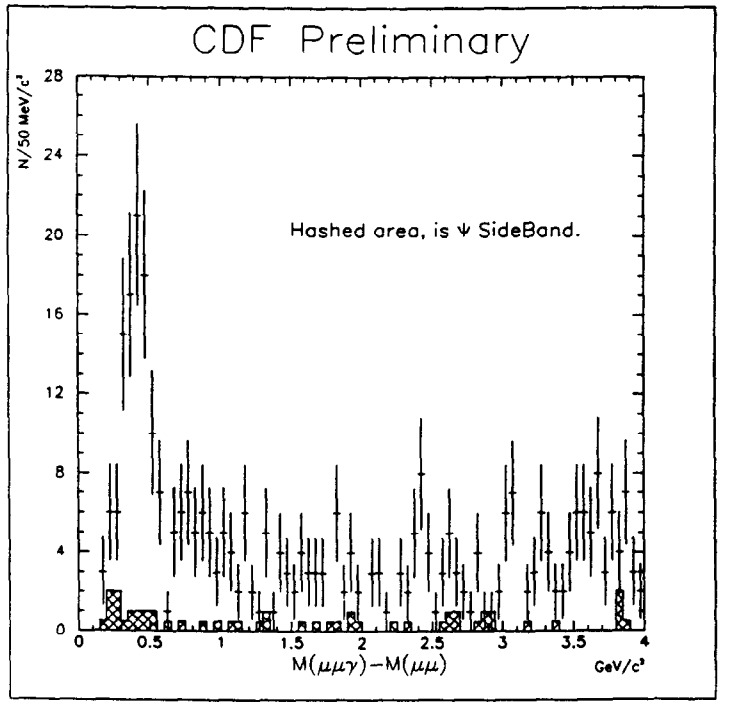

Figure 6: The mass difference M($J/\psi - \gamma$) - M(J/ψ) showing a peak at the value expected for the decay $\chi_{1,2} \rightarrow J/\psi\gamma$.

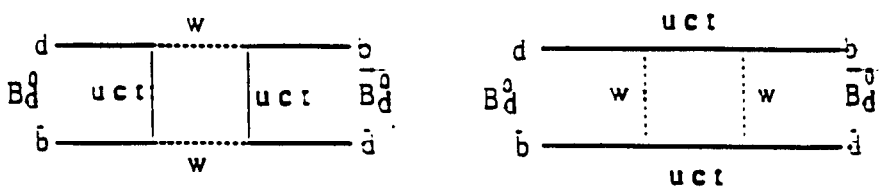

Figure 7: Diagrams contributing to $B^0 - \overline{B^0}$ mixing.

mass region is excluded, and Drell-Yan background is removed by requiring the electrons to be non-isolated. The measured ratios are

$$R_{e-\mu} = 0.552 \pm 0.043(stat.) + 0.39 - 0.48(sys.) \tag{5}$$

$$R_{e-e} = 0.587 \pm 0.113(stat.) \pm 0.043(sys.) \quad . \tag{6}$$

The ISAJET Monte Carlo is used to estimate f_c and f_s allowing extraction of χ. The value determined using both modes combined is

$$\chi = 0.176 \pm 0.031(stat. + sys.) \pm 0.032(MC) \tag{7}$$

where the last uncertainty is due to the Monte Carlo estimates of f_c and f_s. Figure 8 shows the combined result in a plot of χ_d versus χ_s along with the combined result from CLEO and ARGUS [11, 12] The slope of the line from the collider results uses $f_d = 0.375$ and $f_s = 0.15$ to account for the relative fraction of down and strange quark production. The hatched area indicates the region allowed by the Standard Model. The χ_d measurements indicate that χ_s must be large as expected from the Standard Model.

3 Electroweak Measurements

3.1 W and Z Production

Cross sections for W and Z production and decay have been published for electron and muon channels separately [14]. Results from the two channels have been combined assuming universality of couplings to leptons and taking account of correlated errors to yield

$$\sigma \times B(Z^0 \to l^+l^-) = 0.217 \pm 0.021\ nb \tag{8}$$

$$\sigma \times B(W \to l\nu) = 2.23 \pm 0.20\ nb \quad . \tag{9}$$

The values are plotted in Fig. 9 together with data from the UA1 and UA2 [15] experiments at $\sqrt{s}$ =630 GeV, and theoretical predictions [16].

The ratio of these two quantities may be used to extract W leptonic branching fraction from the following relation:

$$R = \frac{\sigma \times B(W \to l\nu)}{\sigma \times B(Z \to ll)} = \frac{\sigma_W \frac{\Gamma(W \to l\nu)}{\Gamma(W)}}{\sigma_Z \frac{\Gamma(Z \to ll)}{\Gamma(Z)}} = 9.98 \pm 0.74 \quad . \tag{10}$$

The ratio σ_W/σ_Z is determined from QCD. Many uncertainties cancel when the ratio is taken. The total and leptonic Z width are obtained from LEP measurements [17]. The measured R then gives

$$\Gamma(W)/\Gamma(W \to l\nu) = 9.67 \pm 0.73 \quad . \tag{11}$$

This ratio is sensitive to possible W decay channels to top, without requiring direct detection of the top quark. Thus it may be used to lower limit on the top mass independent of any top decay mode. In this case the limit obtained is $M_t > 44$ GeV at the 95% confidence level.

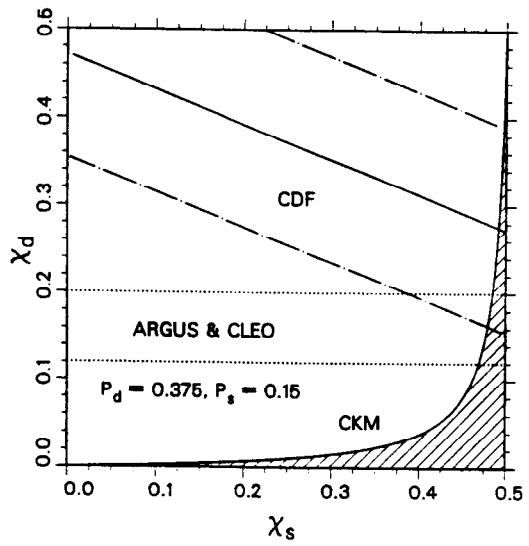

Figure 8: Results on b mixing from CDF, CLEO and ARGUS, showing the results in terms of χ_s and χ_d. The hatched area shows the region allowed by the Standard Model.

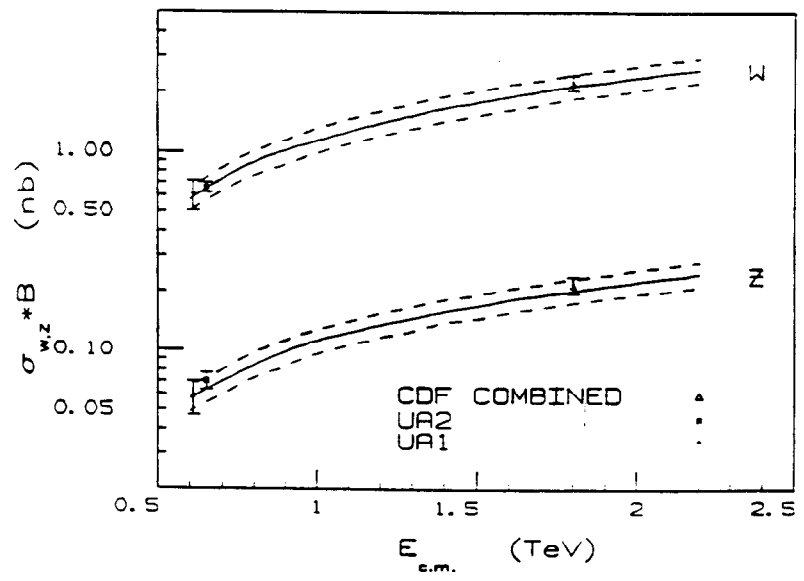

Figure 9: Cross section times leptonic branching ratio for W and Z production for the CDF, UA1 and UA2 experiments along with theoretical predictions.

3.2 $W \rightarrow \tau\overline{\nu}_\tau$

SU(2) gauge invariance in the Standard Model implies a universality of lepton couplings to vector bosons. Measurements at LEP confirm this picture for neutral currents at approximately the 1% level [17]. At hadron colliders, a similar test for charged currents is possible from the decay $W \rightarrow \tau\overline{\nu_\tau}$.

The process $W \rightarrow \tau\nu$ with the τ decaying hadronically gives events with a narrow, low multiplicity jet plus missing E_t. While there are substantial backgrounds from QCD jet production, it is possible to reduce these to a reasonable level. Two triggers were used for this analysis. The first required the missing $E_t > 25$ GeV plus an electromagnetic calorimeter cluster with $E_t > 8$ GeV. The second was a special τ trigger that required missing $E_t > 20$ GeV and a narrow cluster (2 towers) with $E_t > 10$ GeV, with an associated CTC track with $p_t > 4.5$ GeV. Offline, τ clusters were reconstructed by starting with a seed track with $p_t > 5$ GeV. Tracks with $p_t > 1$ GeV within 30^0 of the seed and calorimeter energy within $\Delta\eta \times \Delta\phi$ of 0.6×30^0 were then associated with the seed. The resulting τ clusters were required to have $E_t > 15$ GeV.

Signal τ clusters were taken to be those with ≤ 3 associated tracks and no tracks with $p_t > 1$ GeV between 10^0 and 30^0 of the seed track. Events failing these cuts were considered background. To determine the background in the signal region, these requirements (excluding the event missing E_t requirement) were imposed on a sample of two jet events. This jet sample was normalized to the τ sample for multiplicities ≥ 4 and extrapolated to low multiplicities and subtracted from the signal. A plot of the multiplicity of tracks with $p_t > 1$ GeV/c shows a distinct signal as an excess of 1 and 3 prong tracks (Fig. 10). The overall detection efficiency is determined by Monte Carlo to be $1.61 \pm 0.10\%$ for the missing E_t trigger and $1.72 \pm 0.16\%$ for the τ trigger samples. The combined result for the cross section time branching ratio is

$$\sigma \times B(W \rightarrow \tau\overline{\nu_\tau}) = 2.05 \pm 0.27\ nb \quad . \tag{12}$$

Comparing this to the result for the $e\overline{\nu}$ decay mode of the W gives

$$g_\tau/g_e = 0.97 \pm 0.07 \tag{13}$$

consistent with $e - \tau$ universality.

3.3 High Mass Dilepton Production

In the Standard Model, high mass lepton pairs are produced by the Drell-Yan mechanism including the Z resonance [18]. Deviations from the theoretical distribution could result if leptons either had a composite structure, or from production and decay of a new high mass Z'.

For this study, electron pairs with an invariant mass > 30 GeV were used [19]. To enhance the efficiency, looser requirements were imposed on the second lepton of the pair. Also, looser requirements on the allowed hadronic energy fraction of

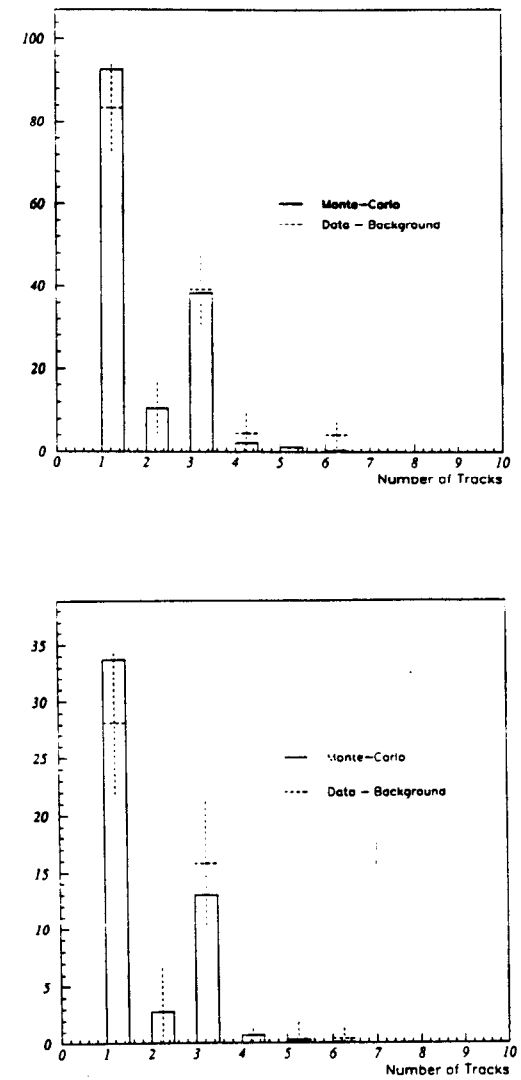

Figure 10: Distribution of charged tracks associated with τ clusters for the missing E_t and τ triggers. The excess of 1 and 3 prong events indicates the τ signal.

electron candidates were made at high E_t to account for increased shower leakage. The primary background is from QCD jets which either fake electrons or produce indirect electrons from conversions or decays. These backgrounds were removed by requiring the electrons to be isolated. The electron identification efficiency was determined using test beam and collider data. The geometric efficiency was determined via Monte Carlo; the total efficiency is 20% for $M = 50$ GeV rising to 50% for $M > 150$ GeV.

The resulting mass distribution is shown in Fig. 11. The integral cross section is shown in Fig. 12, together with the theoretical prediction. If leptons are composite, an effective contact interaction $\mathcal{L}_c = \pm g^2/2\Lambda_{ll}^2(\bar{l}\gamma^\mu l)(\bar{q}\gamma_\mu q)$ produces a flattening of the distribution at high mass. Fitting the distribution to a combined Drell-Yan plus composite interaction gives $\Lambda_{ee}^- > 2.2$ TeV and $\Lambda_{ee}^+ > 1.7$ TeV at the 95% confidence level. Λ is the scale of the effective interaction, the minus sign corresponds to constructive interference and the plus sign to destructive interference with the normal electroweak interaction. A similar analysis of the muon pair mass distribution yields $\Lambda_{\mu\mu}^- > 1.5$ TeV and $\Lambda_{\mu\mu}^+ > 1.3$ TeV at the 95% confidence level.

3.4 Heavy Gauge Boson Production

Heavy gauge bosons arise in many extensions of the Standard Model [20]. A heavy Z' boson would appear as an enhancement in the invariant mass distribution for lepton pairs. Similarly, a heavy W' boson would appear as an excess in the lepton-neutrino transverse mass distribution at high transverse mass.

To search for a Z', the invariant mass distribution for electron and muon pairs is fit to the combination

$$\frac{dN}{dM} = \alpha M(Z') + \beta M(Z^0 + \gamma^*) \tag{14}$$

representing a sum of standard Z, Drell-Yan, and Z' production. Resulting limits on the production cross section times branching ratio to lepton pairs as a function of mass are shown in Fig. 13a. Assuming Standard Model couplings yields a lower limit on the Z' mass of 412 GeV at the 95% confidence level. However couplings of the Z' to quarks and leptons are different from the Standard Model couplings in most extensions. The limit on the production cross section is fairly insensitive to assumptions on the Z' width and couplings to quarks. Predictions of the E_6 model are shown in Fig. 13 b, lower mass limits for a specific model are easily determined from the figure.

Heavy W' bosons are searched for in a similar manner using the lepton-neutrino transverse mass distribution [21]. This distribution is fit to the form

$$\frac{dN}{dM_t} = \alpha M_t(W') + \beta M_t(W) \tag{15}$$

representing a sum of standard W plus W' production. Both electron and muon decay modes are used. The resulting 95% confidence level limit on the produc-

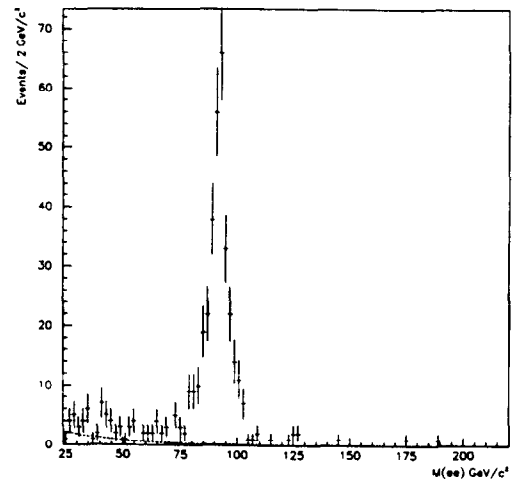

Figure 11: Invariant mass distribution $d\sigma/dM$ for electron pairs.

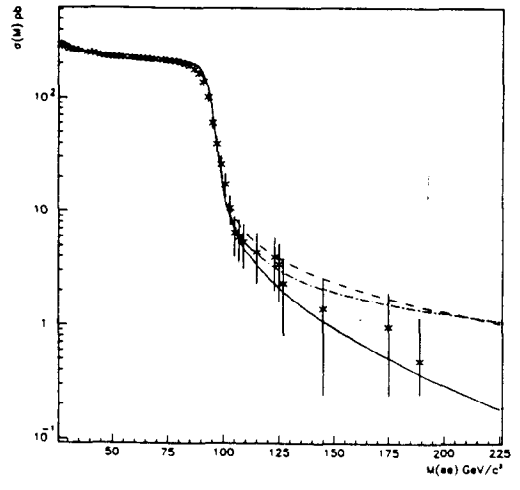

Figure 12: Integral mass distribution $\int_M^\infty d\sigma/dM\ dM$. The solid line is the Standard Model prediction. The dashed line includes a composite interaction with $\Lambda^- = 2.2$ TeV. The dot-dashed line includes a composite interaction with $\Lambda^+ = 1.7$ TeV.

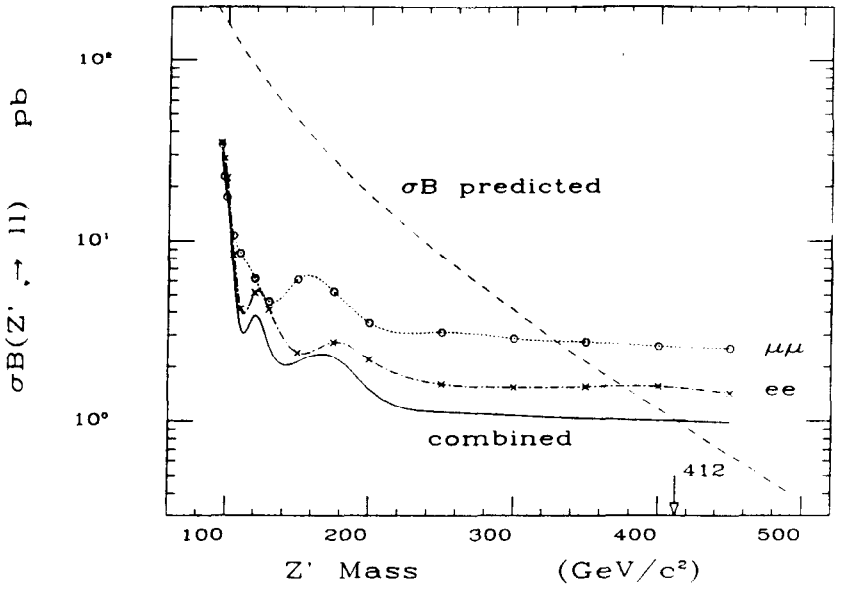

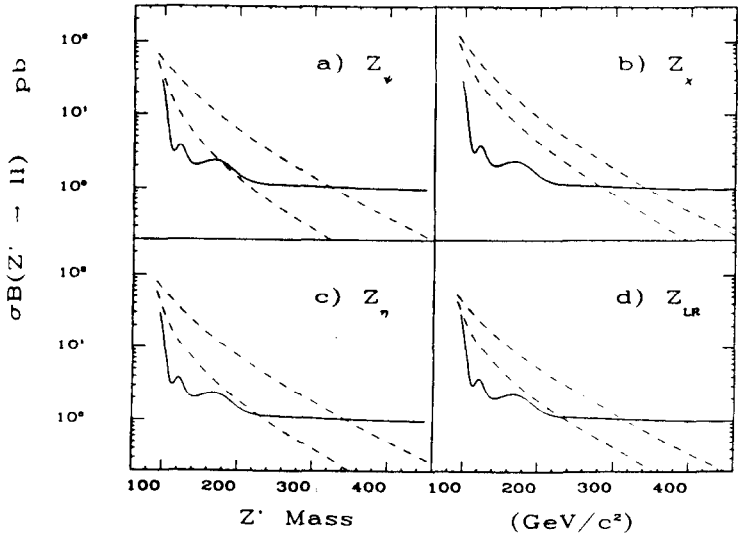

Figure 13: a) Limits on the cross section times branching ratio to lepton pairs for production of Z' bosons. The dashed line is a theoretical prediction assuming Standard Model couplings for the Z'. b) Same as above, but with predictions of the E_6 model for various assumptions about mixing parameters. The upper curve in each plot is the prediction assuming no s-fermion channels are allowed. The lower curve is the prediction assuming all possible s-fermion channels are allowed.

tion cross section times branching ratio to lepton-neutrino is shown in Fig. 14. Assuming Standard Model couplings gives a lower limit $M(W') > 520$ at the 95% confidence level.

4 Particle Searches

4.1 Search for the Top Quark

Top is produced in $\bar{p}p$ collisions via $\bar{p}p \to \bar{t}t + X$, where the t then decays into Wb. The W then can decay into a $\bar{q}q$ pair, or $l\bar{\nu}$. Because of large QCD backgrounds, searches are limited to channels where one or both W's decays to a lepton. The dilepton mode is the cleanest, but has the smallest branching fractions (2/81 for $e\mu$, and 1/81 for ee or $\mu\mu$). The channel for $\bar{t}t$ into leptons plus jets has a larger branching fraction, but there is a substantial background from high p_t W production with associated jets.

The CDF search combines the $e\mu$ ee, $\mu\mu$, W plus jets and W plus jets where one of the jets has a soft μ from b decays [22]. The 95% C.L. limit on $\sigma(\bar{t}t)$ is shown in Fig. 15 for each of the processes. The intersection of the curves with the lower limit of the theory cross section gives the limit on the top mass, 89 GeV. Note however it is not valid for models in which top does not decay with standard couplings (*e.g.*, charged Higgs).

4.2 Search for Supersymmetry

Supersymmetry is a proposed symmetry where each fermion (boson) has a corresponding supersymmetric boson (fermion). Quarks, gluons, and photons have as their supersymmetric partners the squark ($\tilde{q}$), gluino ($\tilde{g}$), and photino ($\tilde{\gamma}$). Conservation of a SUSY quantum number implies that the lightest supersymmetric particle is stable and will escape detection. Because of this, expected signatures of supersymmetry will include substantial missing E_t. The gluino decays according to $\tilde{g} \to q\bar{q}\tilde{\gamma}$. Squarks either decay according to $\tilde{q} \to q\tilde{g}$ or $q\tilde{\gamma}$ depending of the relative masses of the squark and gluino.

Assuming the case $m_{\tilde{q}} < m_{\tilde{g}}$, events were selected with 2 jets with $E_t > 15$ GeV and a missing $E_t > 100$ GeV. Three events were observed with an expected background of 1.3 events. For the case where $m_{\tilde{g}} < m_{\tilde{q}}$, four jets with $E_t > 15$ GeV were required with a missing $E_t > 40$ GeV. Two events were observed, again with an expected background of 1.3 events. These results give the limits on squark and gluino masses shown in Fig. 16 [23]. Possible cascade decays of the squark and gluino would reduce these mass limits by ≈ 30 GeV [24].

4.3 Search for Heavy Stable Particles

Heavy stable particles are possible in some theories that go beyond the standard model [25]. CDF has performed a search for heavy, penetrating particles that live

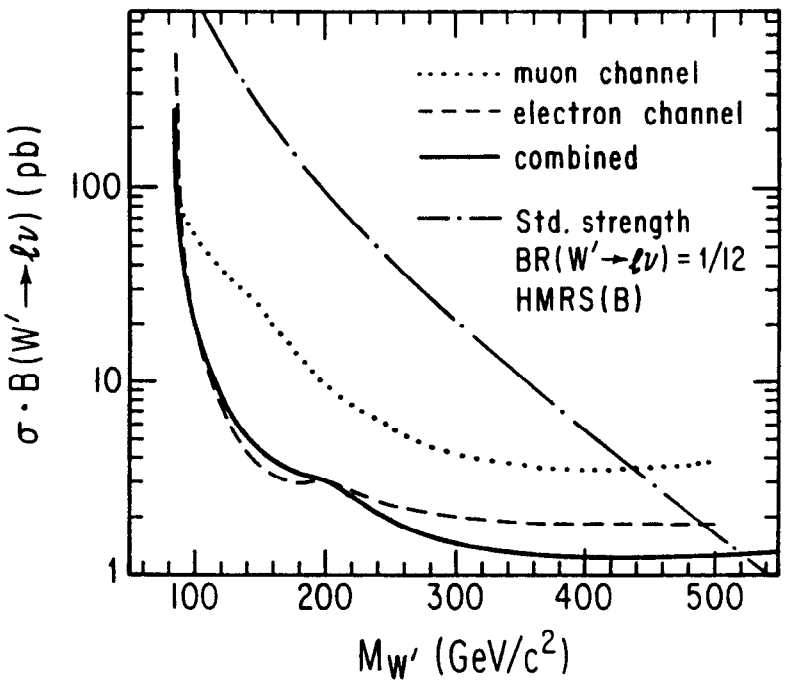

Figure 14: Limit on cross section times branching ratio for production of W' bosons. The solid line is a theoretical prediction assuming standard couplings for the W'

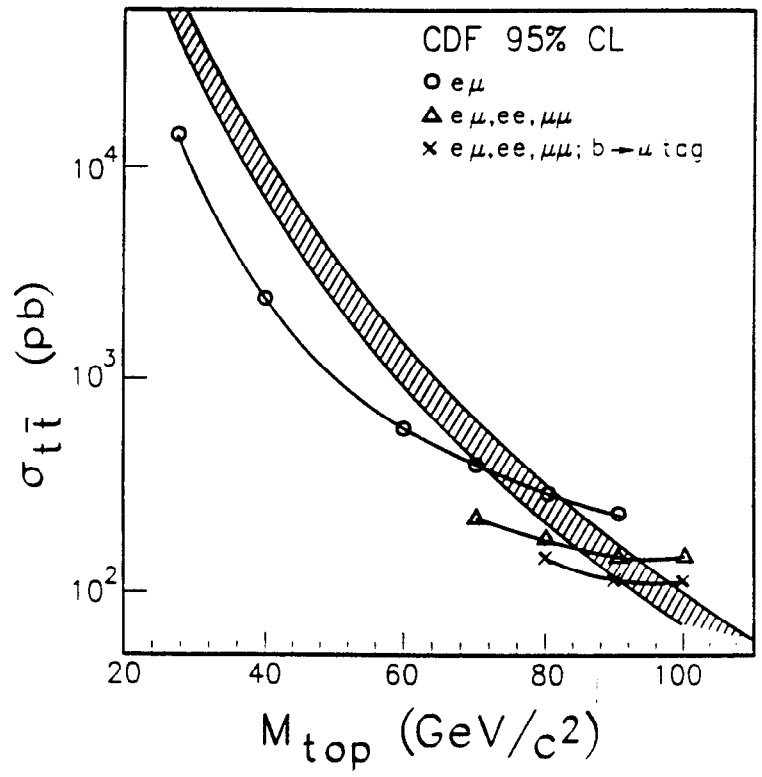

Figure 15: 95% C.L. limit on top quark production cross section together with theoretical predictions. The lower mass limit of 89 GeV is derived from the intersection of the 95% C.L. limits with the theoretical prediction plus uncertainty (band).

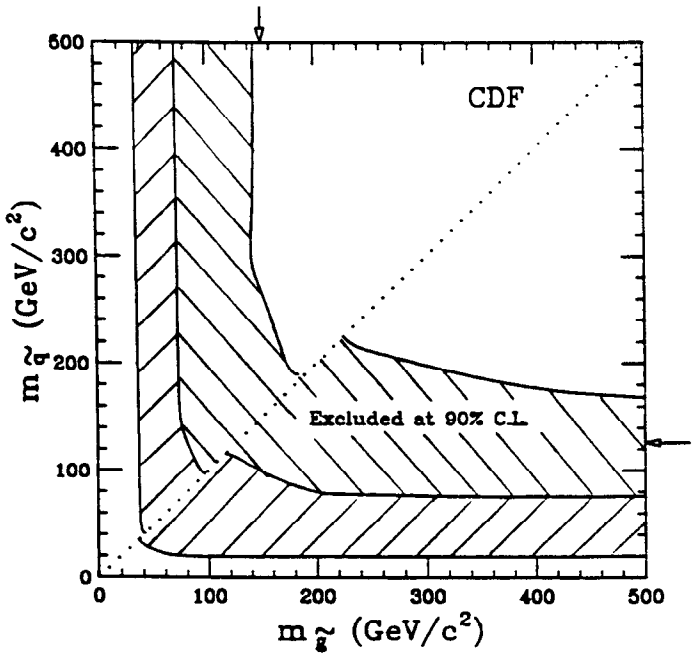

Figure 16: Limits on the masses of squarks and gluinos. The upper left half corresponds to the case $m_{\tilde{q}} < m_{\tilde{g}}$. The lower right of the diagonal corresponds to $m_{\tilde{g}} < m_{\tilde{q}}$.

long enough to traverse the detector ($\tau > 10^{-8}$ sec.) [26]. Particles are detected in the central muon system, the velocity is determined from the momentum measured by the CTC and timing information from the hadron calorimeter. This timing information has a resolution of 1.6 ns. The dominant systematic uncertainty is the determination of the appropriate path length given the large depth (120 cm) of the hadron calorimeter.

Candidate tracks were required to have $p_t > 25$ GeV, $0.5 < \beta < 0.65$, and have energy deposition in the calorimeter consistent with their velocity. The lower velocity requirement prevents most tracks from ranging out in the calorimeter. The upper requirement selects tracks so that the scintillator light output stays ahead of the track providing a clean definition of the path length. One candidate event survives these cuts; the estimated background is 2.3 ± 1.3 events. Monte Carlo simulations were used to derive the detection efficiency for such particles. This gives the limit on the production cross section at the 95% confidence level shown in Fig. 17.

This limit is compared to the predictions of several theoretical models. For the spin 1/2 color triplet model of Ellis, masses between 50 and 139 GeV are ruled out at the 95% confidence level. Other models including color sextets, octets, and decuplets with resulting mass limits of 224, 227, and 290 GeV were also considered. Spin 0 color triplets are excluded in the mass range between 50 and 85 GeV. The search was extended to include charge 2/3 and 4/3 particles. One event survived the cuts for the charge 2/3 sample and 2 for the charge 4/3 sample. Both are consistent with the estimated backgrounds of 0.8 ± 0.8 and 1.5 ± 1.1 events respectively. Masses between 50 and 116 GeV are ruled out at the 95% confidence level for the charge 2/3 case and masses between 50 and 140 GeV for the charge 4/3 case. If one accounts for possible production of neutral as well as charged particles, these limits would be lowered by about 20 GeV.

5 Tests of QCD

5.1 Inclusive Jet Production

Past studies of jet production at $\bar{p}p$ colliders have shown reasonable agreement with leading order QCD calculations [29, 31, 30]. However, comparisons have been limited by large theoretical uncertainties in those calculations due to the dependence on the renormalization scale μ^2. Recently, $\mathcal{O}(\alpha_s^3)$ calculations have been performed substantially improving the theoretical precision [32, 33]. The calculations include diagrams with up to three partons in the final state. To deal with divergences arising from soft or collinear partons, partons are combined into a single "jet" if they fall within some cone in $\eta - \phi$ space. Jet variables are determined from

$$E_t^{jet} = \sum_{R_i \leq R_0} E_{ti}; \; \eta^{jet} = \sum_{R_i \leq R_0} E_{ti}\eta_i; \; \phi^{jet} = \sum_{R_i \leq R_0} E_{ti}\phi_i \quad . \tag{16}$$

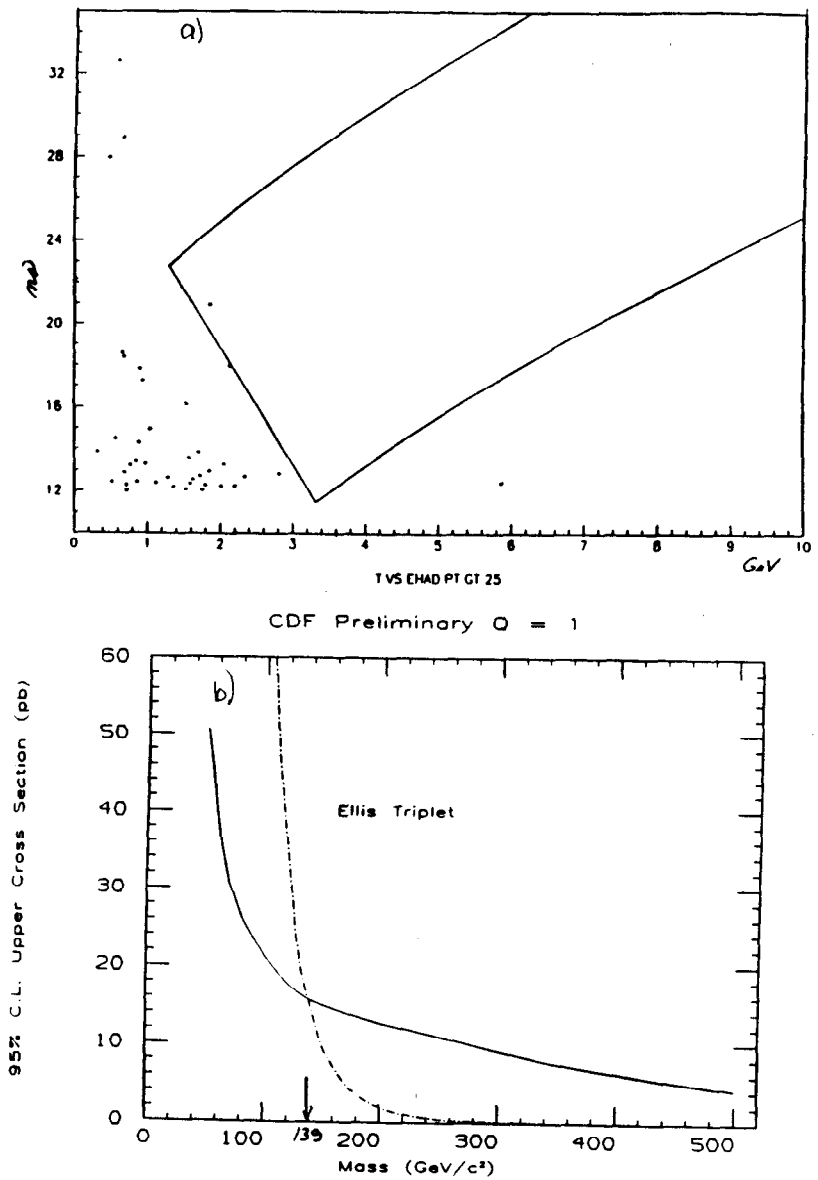

Figure 17: a) Time of flight in ns versus energy deposition in the calorimeter for candidate heavy stable particles. The band corresponds to the range $0.5 < \beta < 0.65$. b) Limits of the production cross section for charge 1 stable particles, together with predictions of the Ellis color triplet model.

This is analogous to the experimental jet definition, where jets are clusters of energy within a fixed cone in $\eta - \phi$ space [34].

Measurement of the inclusive single jet E_t distribution is restricted to central region ($0.1 < |\eta| < 0.7$). This region has best known energy scale and resolution, giving the least systematic uncertainty. The observed jet energies must be corrected for the calorimeter response, cracks, leakage, and the underlying event. No correction is made for energy not included in the clustering cone; this is accounted for by the QCD calculation. The calorimeter response was measured in a test beam of electrons and pions for the energy range 3 GeV to 150 GeV. For lower energy particles, isolated tracks in minimum bias events were used. The particle momentum measured using the central tracking chamber was compared to the energy in the calorimeter region pointed to by the track. The ISAJET Monte Carlo plus detector simulation was tuned to reproduce the observed particle multiplicity and momentum distributions, and the calorimeter response. The total jet energy correction ranges from $50 \pm 12\%$ for a jet with $E_t = 30$ GeV to $15 \pm 5\%$ for a jet with $E_t = 300$ GeV.

In addition to correcting observed jet energies as described above, the steeply falling distribution must be corrected for resolution effects. Figure 18 shows the resulting distribution compared to the NLO QCD calculation. The total systematic uncertainty ranges from $\pm 60\%$ at $E_t = 50$ GeV to $\pm 22\%$ for $E_t > 80$ GeV. The agreement is seen to be good over 7 orders of magnitude in cross section. The fractional difference between the data and theory is shown in Fig. 18 for several choices of structure functions. The HMRSB[27] and MT[28] structure functions give acceptable fits to the data, but the HMRSE set gives a poor fit.

The NLO calculations predict the cross section as a function of the jet cone size R. This is shown in Fig. 19 for jets with $E_t = 100$ GeV. The three curves represent different choices of the renormalization scale μ^2. It is seen that there is still some dependence of the calculation on the choice of renormalization scale. However this appears to be minimized for a cone size of 0.7.

If quarks had a substructure, then one might expect a binding force of the constituent particles to become evident at very short distances. This may be parameterized by a 4-Fermi term to be added to the interaction Lagrangian. In the case of $q\bar{q} \to q\bar{q}$ scattering, this is:

$$\mathcal{L}_c = \frac{g^2}{2\Lambda_c^2}(\bar{q}\gamma^\mu q)(\bar{q}\gamma_\mu q) \quad . \tag{17}$$

The effect of such an interaction would be to increase the rate of jet production at high E_t causing a flattening of the distribution. A fit to the above inclusive E_t distribution including the 4-fermi interaction gives a lower limit of 1.4 TeV at 95% confidence level on Λ_c. Note that the NLO calculation cannot be done with an added 4-fermi interaction. Hence the fit is done at leading order, with the associated theoretical uncertainty included in the limit.

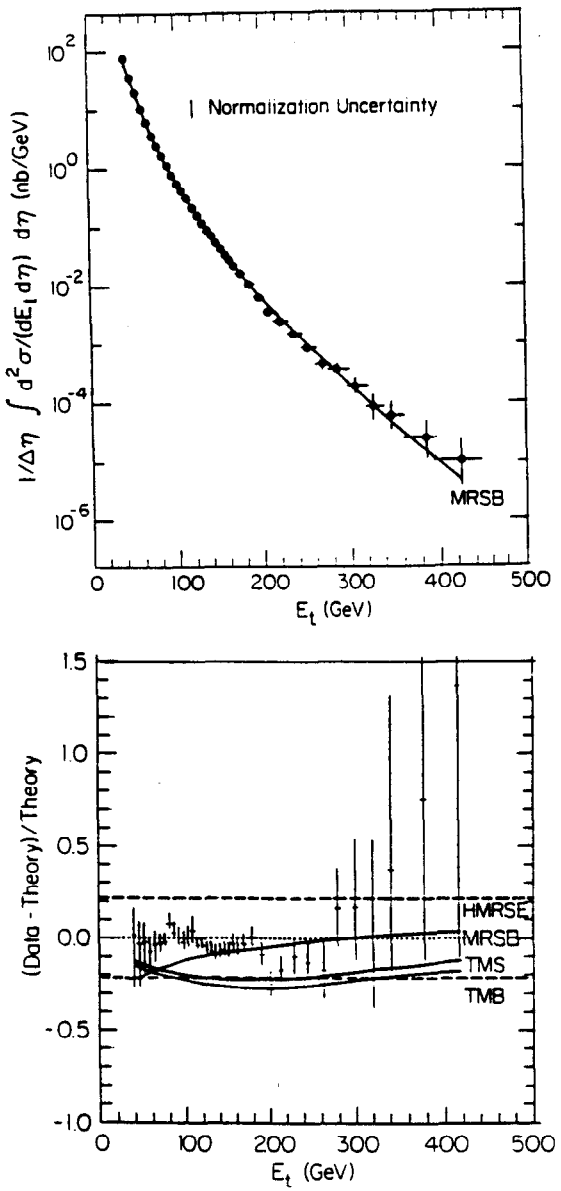

Figure 18: Inclusive jet cross section as a function of E_t compared to the predictions of an $\mathcal{O}(\alpha_s^3)$ QCD prediction [32, 33]. All normalizations are absolute. Also shown is the ratio of (data-theory)/theory plotted for different choices of structure functions.

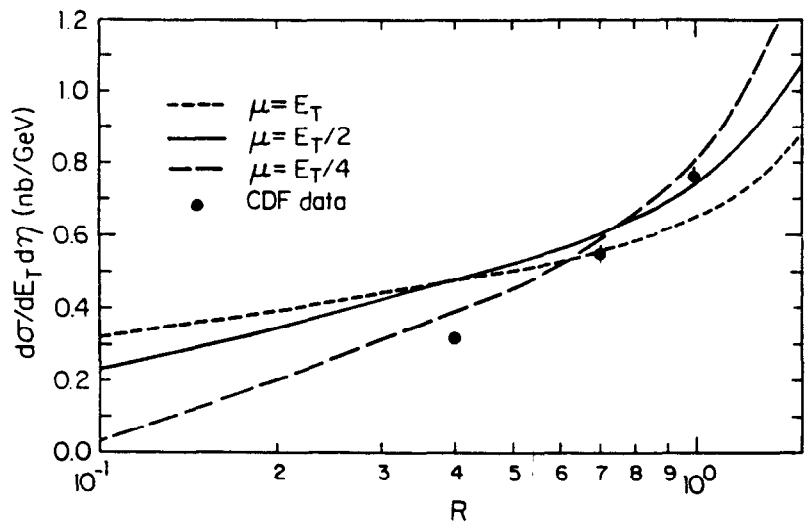

Figure 19: Variation of the CDF jet cross section for $E_t = 100$ GeV with cone radius R. The curves are NLO predictions for several choices of the renormalization scale μ^2.

5.2 Jet Shapes

Next to Leading Order calculations are available that describe the energy distribution in the jet cone [35]. This is parameterized by the fraction of the jet energy within an inner cone of radius r $\rho(r)$. This is measured by the CDF detector using tracks due to their better spacial and momentum resolution for single particles. Figure 20 shows this distribution for 100 GeV jets. Also shown are the $\mathcal{O}(\alpha_s^3)$ predictions [35], along with the predictions of the event generator HERWIG [36]. The agreement is surprisingly good; no fragmentation effects are included in the calculation. Note there still is some dependence on the choice of renormalization scale.

5.3 Two Jet Mass Distribution

The two jet invariant mass distribution has also been measured; this provides a further test of QCD, and also could exhibit modifications due to production of high mass states decaying into two jets. To obtain the best resolution, jets were required to satisfy $|\eta| < 0.7$. For this measurement, rather than correct the data for the energy resolution, the theory is smeared by the experimental resolution. Results are shown in Fig. 21 for cone sizes of 1.0 and 0.7. The agreement is good for the 1.0 cone, but poorer for the cone size of 0.7. However Next to Leading Order calculations are now available [37]; early indications are that they give somewhat better agreement between the data and theory.

5.4 Two Jet Angular Distribution

Also measured is the jet angular distribution in the jet center of mass frame. To insure an approximately uniform acceptance, requirements are imposed on the variables $\eta_b = (\eta_1 + \eta_2)/2$ and $\eta^* = (\eta_1 - \eta_2)/2$ where η_1 and η_2 are the pseudorapidities of the two highest E_t jets. Specifically, the requirements $|\eta_b| < 0.75$ and $|\eta^*| < 1.6$ are imposed. The center of mass scattering angle θ^* is related to η^* by $\cos\theta^* = \tanh\eta^*$. To ensure a fully efficient trigger over the angular range, the data is divided into mass windows of $240 < M_{JJ} < 475$ GeV, $475 < M_{JJ} < 550$ GeV, and 550 GeV $< M_{JJ}$. For comparison to theory, the angular distribution is plotted in terms of the variable $\chi = (1 + |\cos\theta^*|)/(1 - |\cos\theta^*|)$. This distribution is expected to be approximately flat for the dominant t-channel exchange process and thus insensitive to smearing effects. The data are shown in Fig. 22 for the three mass regions together with predictions of Leading Order QCD based on the HMRSB and M-T structure functions. For the HMRSB case, Next to Leading Order QCD [38] calculations are also shown. The NLO calculations fit the data somewhat better in that case, however the LO calculations with the M-T structure functions provide an equivalently good fit to the data.

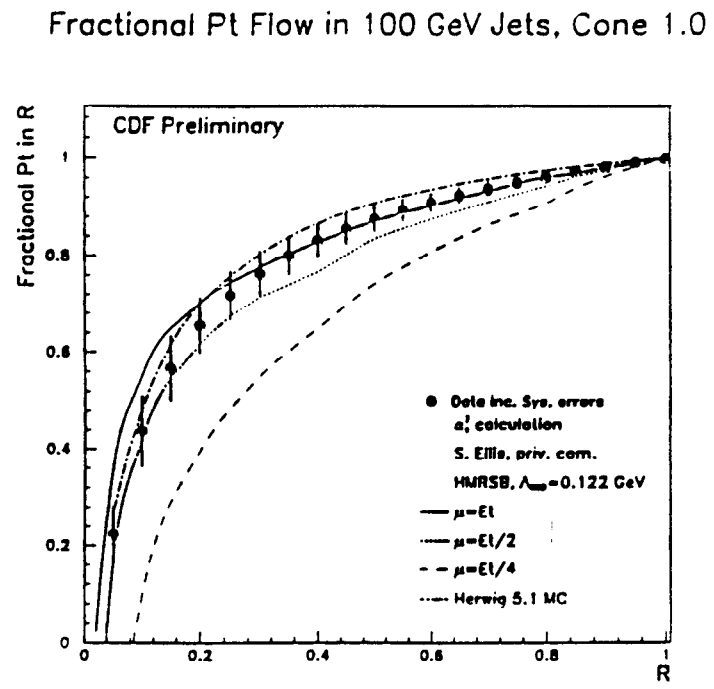

Figure 20: Jet shape, $\rho(r)$ (defined in text) for 100 GeV E_t jets from CDF. The curves are from an $\mathcal{O}(\alpha_s^3)$ parton level calculation, and also from the HERWIG event generator [36].

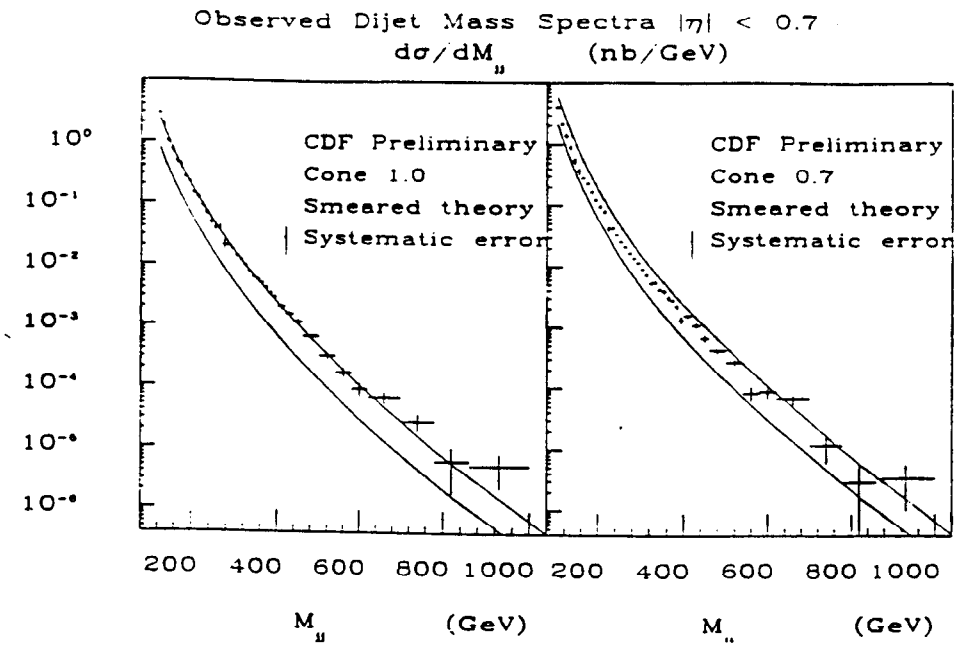

Figure 21: The two jet invariant mass distribution. The band enclosed by solid lines is a calculation based on leading order QCD.

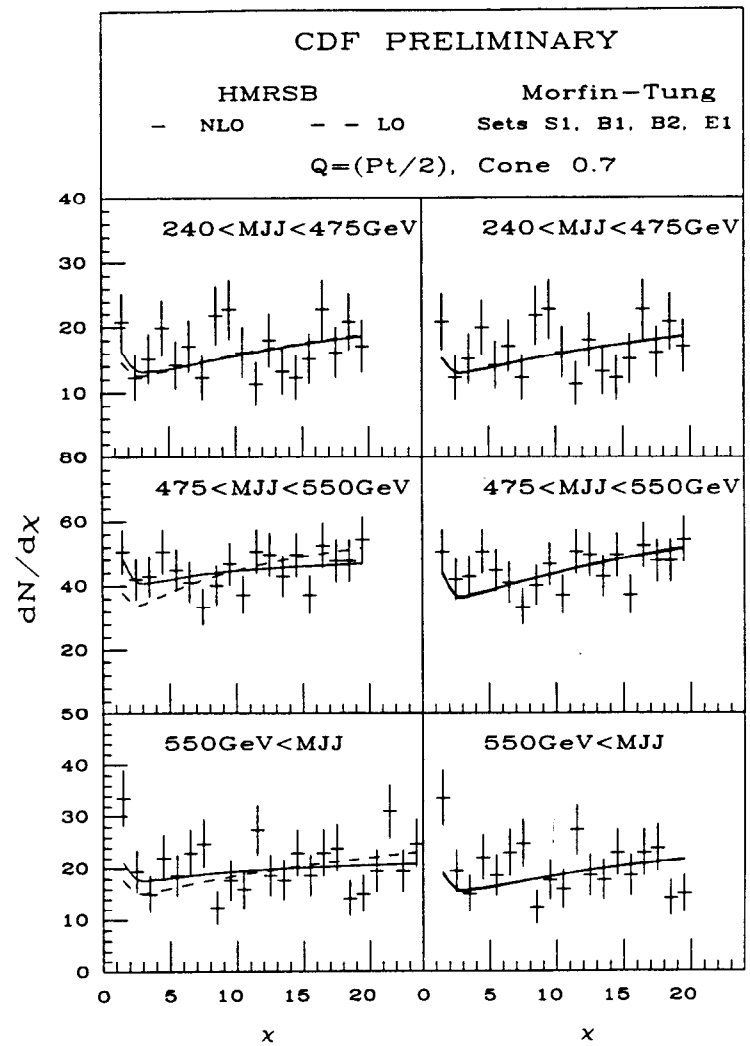

Figure 22: Center of mass angular distribution for two jet events. Also shown are calculations based on leading order QCD based on HMRSB and M-T structure functions. For the HMRSB case, NLO QCD calculations are also shown.

5.5 Three Jet Production

The kinematics of 3 jet final states have been measured and compared to tree level QCD predictions [39]. Four independent variables describe the kinematics. These are taken to be θ^*, the angle of the leading jet with respect to the beam axis; ψ, the angle between the planes containing the beam and leading jet (designated parton 3); the plane containing the two subleading jets (partons 4 and 5), and the jet energies scaled to the center of mass energy, $x_i = 2p_i/\sqrt{\hat{s}}$ $(x_3 + x_4 + x_5 = 2)$.

Events are selected with at least three jets each with $E_t > 15$ GeV. The event is boosted to the center of mass frame, and the jets ordered by energy in this frame. The following additional selection criteria are imposed to produce an event sample for which the detector acceptance is approximately uniform:

- $|\cos\theta^*| \leq 0.6$,
- $\sqrt{\hat{s}} \geq 250$ GeV,
- $30° \leq \psi \leq 150°$,
- $x_3 \leq 0.9$.

Following application of the cuts, 4826 events remain. Tree level matrix elements [40, 41] are used to generate events to a detector simulation, where they are subjected to the same cuts as the data. Figure 23 shows the measured distributions together with the QCD predictions and also a QCD prediction for quark-only initial states. Also shown is a Monte Carlo preduction assuming a phase space distribution for the three jets. The agreement of the data with the QCD calculation is good. The data are not consistent with the phase space distribution.

A global fit to all four distributions was made where the $\bar{q}q$ fraction in the initial state is fitted as a free parameter. The result is 3^{+7}_{-3} %, consistent with the tree level prediction of 11±4 %. The total cross section, given the event selection is 1.2 ± 0.02 (stat) ± 0.6 (syst) nb, whereas the tree level prediction is 1.8±0.9 nb.

5.6 High P_t W and Z Production

W and Z production is described in leading order in perturbation theory by the Drell-Yan mechanism. At higher orders, the W and Z can recoil against a quark or gluon to obtain a finite kick in the transverse plane. When the W p_t is large enough, the leading terms in perturbation theory should give a reasonable description of the data. For small W or Z p_t's, one must rely on a summation of leading terms from soft gluons to all orders to obtain the cross section [42].

The W p_t distribution must be corrected for the missing E_t carried away by the neutrino, and an unfolding procedure must be applied to take into account the effect of the jet energy resolution on the steeply falling spectrum [43]. The Z p_t distribution can be measured more accurately, because the e^+e^- can be measured fairly precisely, but suffers from lower statistics [44]. The results are shown in Fig.

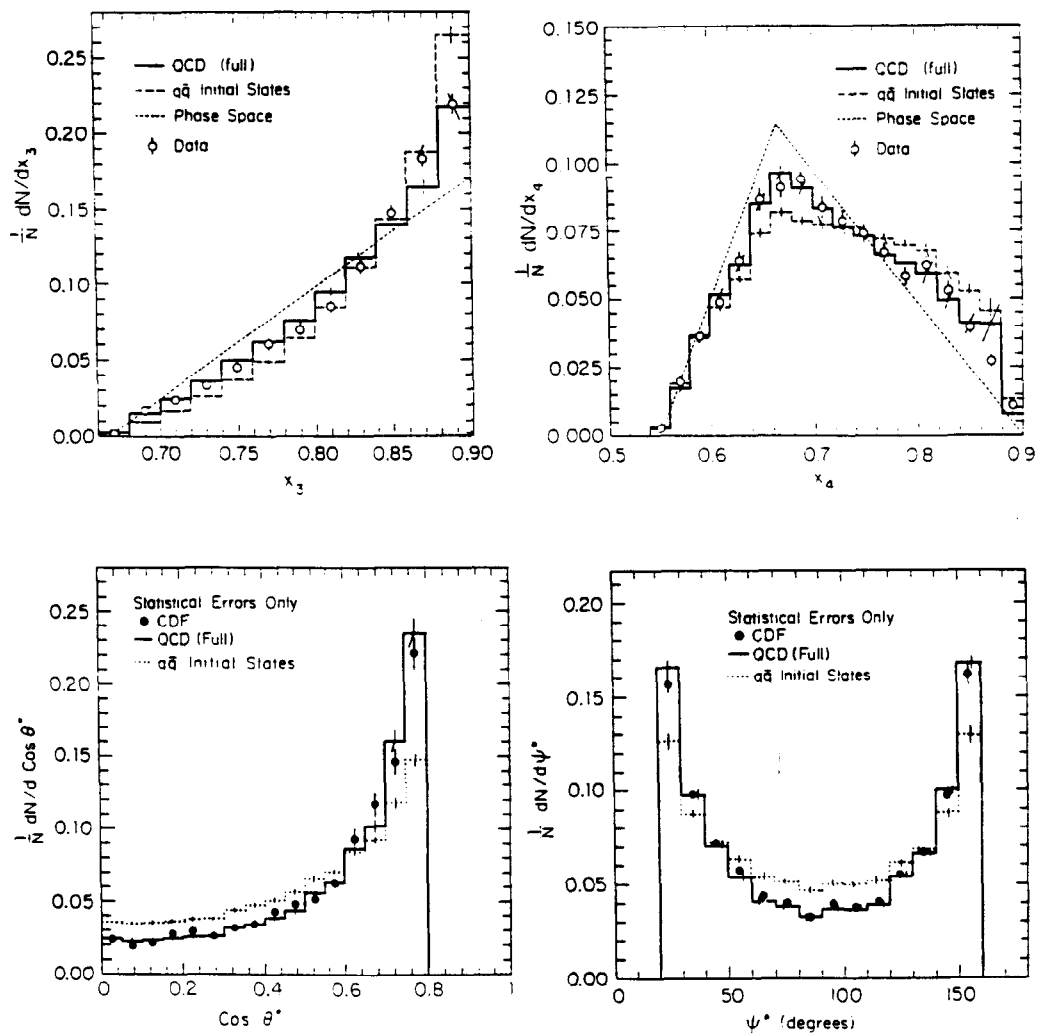

Figure 23: Variables for three jet events, x_3, x_4, $\cos\theta^*$ and ψ^*, showing the data, the predictions of QCD, and the prediction from $\bar{q}q$ initial states only. The data are compatible with the small expected fraction of $\bar{q}q$ in the initial states.

24. The QCD predictions at Next to Leading Order [42], $\mathcal{O}(\alpha_s^2, \alpha_{em})$, provide a good description of the data, and there is no significant excess apparent at high p_t.

5.7 Direct Photon Production

In principle, direct photon production $\sigma(\bar{p}p \rightarrow \gamma + X)$, provides a particularly clean test of QCD. The energy of the photon is well measured by the electromagnetic calorimeter, and there are no fragmentation effects. Next to Leading Order calculations are not as difficult as for the jet case, and have been performed by Aurenche and others [45, 46, 47]. At low photon energies, this process also provides a good probe of the gluon structure function. However the measurement is complicated by the difficulty of separating single photons from high energy π^0's where the two photons are highly overlapped.

It is not possible to separate π^0's and photons on an event by event basis. Instead, a statistical method using the shower profile in the central strip chambers is employed. Showers from π^0 decays will tend to have a broader profile. Measured profiles are compared to those expected for single photons and a χ^2 computed. The standard profiles are obtained from test beam electron showers, and photon showers from reconstructed $\eta \rightarrow \gamma\gamma$ decays. This method achieves reasonable separation for $E_t < 40$ GeV, above which π^0's are too collimated. Also, an isolation cut requiring $< 0.1E_\gamma$ additional energy within a cone of 0.7 in $\eta - \phi$ space about the photon candidate is made to further reduce the backgrounds.

To extend the measurement above E_t of 40 GeV, and also as a cross check on the lower E_t measurements, a conversion method is employed. This uses the outer wall of the central tracking chamber as a photon converter ($\approx 0.2X_0$), followed by a series of drift tubes which provide information on the conversions. The conversion probability for photons is roughly constant as a function of photon energy, and hence a statistical subtraction of the π^o (and η) contribution is possible up to relatively high photon E_t. This method is limited by statistics due to the small wall thickness.

The results for the cross section as a function of E_t are displayed in Fig. 25, along with the predictions of a Next to Leading Order QCD prediction by Aurenche *et al.* [45]. The data appear to be running higher than the indicated predictions at low E_t. The calculations are not evaluated fully at $\mathcal{O}(\alpha_s^2, \alpha_{em})$ as the contribution from bremsstrahlung off of quark lines is only approximated. It is possible that a full calculation may improve the comparison between theory and experiment.

The angular distribution in the γ - jet center of mass system has also been measured. The method is similar to the two jet angular distribution described previously. Regions in the $\eta^* - \eta_b$ plane are selected to to insure an approximately uniform acceptance in $\cos\theta^*$. The result is shown in Fig. 25, along with the distribution from jet-jet events in a similar kinematic range. Because the γ–jet events come predominantly from spin-$\frac{1}{2}$ quark exchange, the angular distribution is not

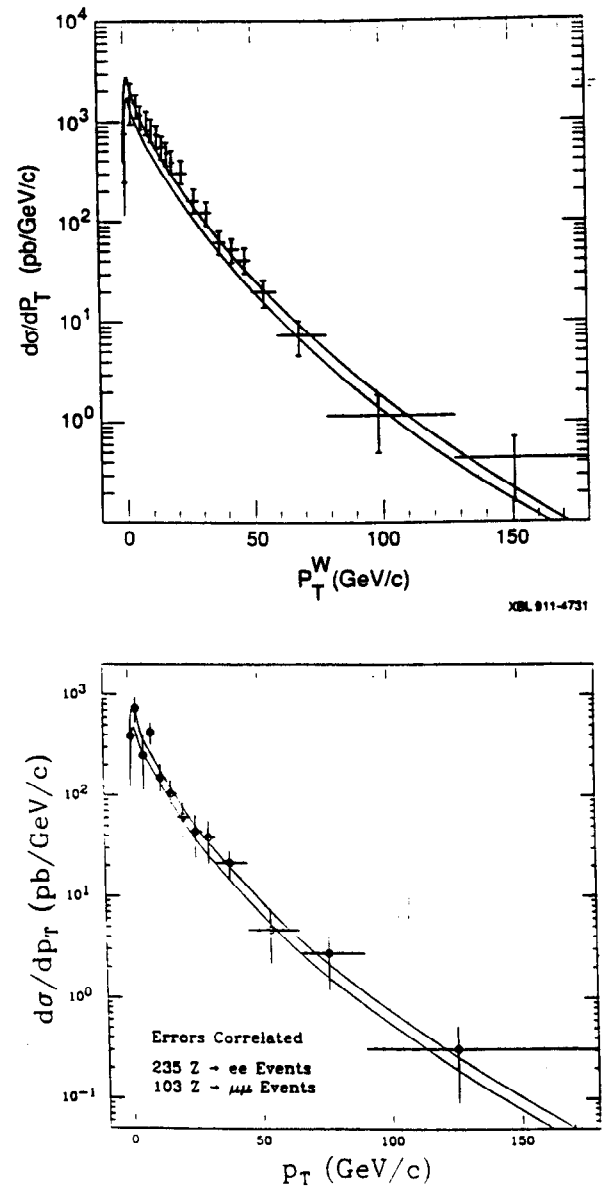

Figure 24: p_t distributions for W and Z bosons. The curves are theoretical predictions of Arnold, Kauffman and Reno [42].

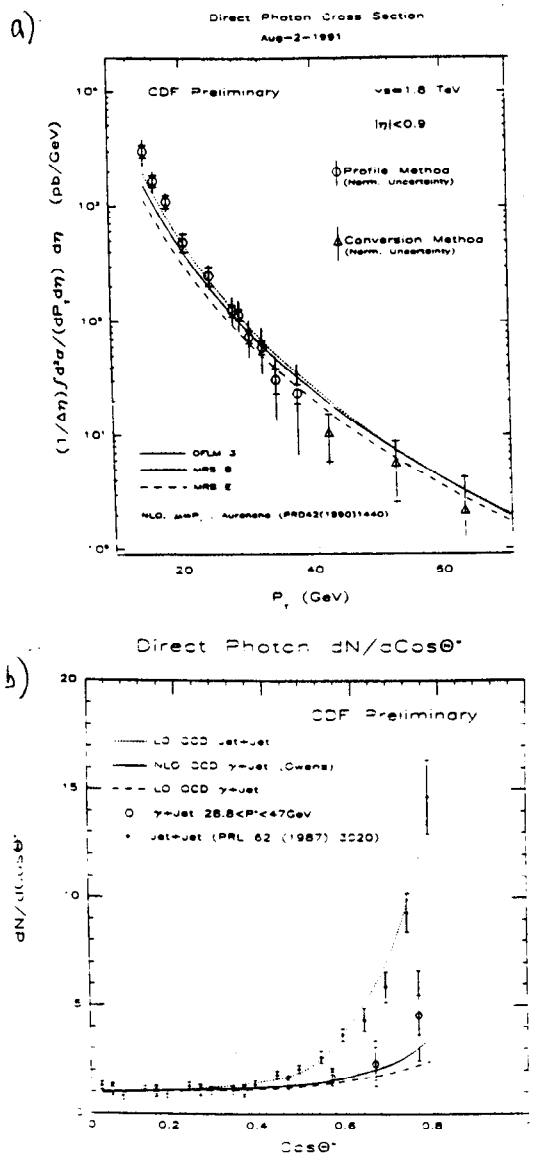

Figure 25: a) Inclusive direct photon cross section versus E_t. The lines are the predictions of a Next to Leading Order QCD prediction. b) The γ - jet angular distribution in the center of mass frame ($\cos\theta^*$). Also shown is the jet-jet angular distribution, measured in a similar kinematic range. The QCD predictions for both processes are indicated.

the same as for jet-jet scattering, which is dominated by spin-1 gluon exchange at small angles.

Two photons may be produced according to the diagrams in Fig. 26. They are refered to as the Born diagram ($qq \rightarrow \gamma\gamma$), the box diagram ($gg \rightarrow \gamma\gamma$) and bremsstrahlung diagrams. For events with two photon candidates, the profile method subtraction described above is used to estimate the number of true two photon events. For photons with $10 < E_t < 35$ GeV, there are 149 candidate events. Roughly one-third are true di-photon events. Figure 27 shows the cross section as a function of the E_t of each photon. This is compared to a calculation using the PYTHIA Monte Carlo, which includes only the Born and box diagrams. The data is in qualitative agreement with the incomplete calculations.

6 Total Cross Section

The total cross section, $\sigma_t(\bar{p}p)$ may be written using the optical theorem

$$\sigma_{tot}^2 = 16\pi(1+\rho^2)^{-1}\frac{d\sigma^{el}}{dt}|t=0 \tag{18}$$

where ρ is the ratio of the imaginary to real part of the forward scattering amplitude. The parameter ρ at low energies is typically less than 0.1; however an anomalously high measurement of $\rho = 0.24 \pm 0.04$ has been reported by the UA4 collaboration [48] (CMS energy of 630 GeV). However the E710 collaboration has reported a measurement of ρ that is more consistent with expectations [49].

To determine the total cross section, the elastic cross section as a function of the 4-momentum transfer squared t was measured. The cross section depends exponentially on t for low t, the measurement is extrapolated to $t = 0$ to determine the forward scattering amplitude. Since the phase is not measured, an assumption must be made about the value of ρ, and the uncertainty included in the systematic error.

The CDF detector included chambers near the beamline for detection of scattered elastic tracks. The luminosity was determined by careful measurement of the accelerator parameters, with an estimated uncertainty of $\pm$ 6.8%. A value of $\sigma_t = 71.5 \pm 3.0$ mb is found, assuming $\rho = 0.145$ [50]. A wide range of ρ ($0.1 < \rho < 0.2$) is included in the systematic uncertainty. The results from both E710 and CDF are consistent and show a preference for an asymptotically flat extrapolation over an asymptotic form of $log^2(s/s_o)$ [51].

7 Summary

B production has been observed at a rate comparable to or greater than the theoretically predicted rate. Exclusive decays of B mesons have been reconstructed for the first time at a hadron collider. Measurements of electroweak parameters, jet and photon production are generally in agreement with the standard model.

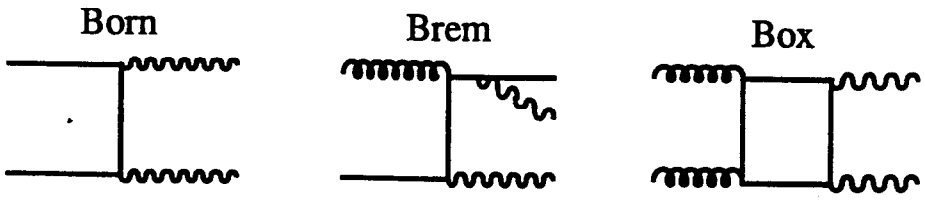

Figure 26: Diagrams for lowest order double direct photon production.

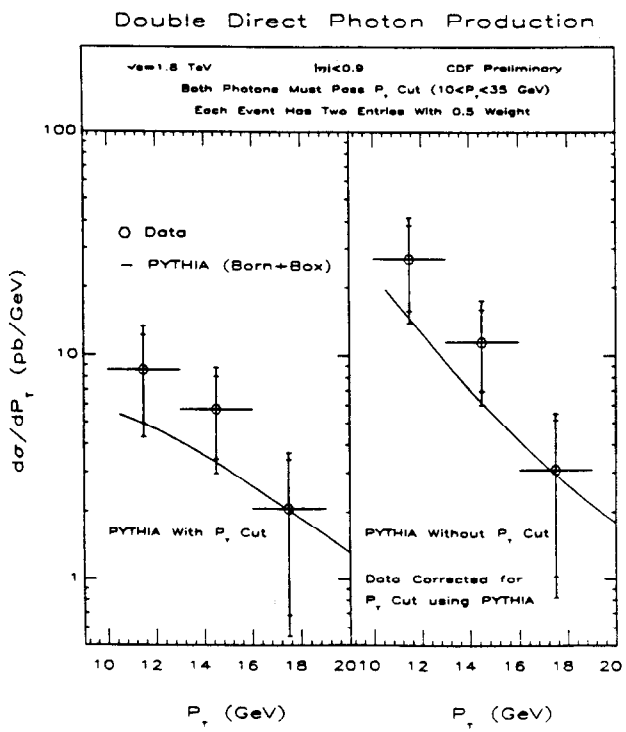

Figure 27: The isolated double direct photon cross section compared to PYTHIA (left) with an E_t cut on each photon. (right) without an E_t cut on each photon, with the data corrected according to PYTHIA.

No evidence for top, heavy stable particle, or supersymmetric particle production has been observed and stringent limits have been established.

The next run of the Tevatron Collider is scheduled to begin in early 1992. Improvements in the accelerator are expected to increase the peak luminosity by perhaps a factor of 5, to $10^{31}/cm^2/sec$. The goal is to record at least 25 pb^{-1} during this run. During this run the D0 detector will be operational for the first time.

Several improvements are being made to the CDF detector. A silicon strip detector with 4 layers and an active length of $\approx$ 50 cm is being installed to detect secondary vertices from short lived particles. The vertex TPC system is being replaced by chambers with a shorter drift space to cope with positive ion buildup effects from the higher luminosity. Preradiator chambers are being installed in front of the central electromagnetic calorimeter to improve photon detection. Central muon coverage is being extended to $\eta = 0.9$, and additional steel is being added for $\eta < 0.5$.

8 Acknowledgements

I wish to thank my colleagues in the CDF collaboration, whose dedicated efforts have made these results available, for their assistance in preparing this report. I also thank the organizers of the SLAC Summer Institute for their hospitality.

References

[1] F. Abe *et al.*, Nucl. Inst. Meth. **A271**, 387 (1988) and references therein.

[2] P. Nason, S. Dawson and R.K. Ellis, Nucl. Phys. **B303** 607 (1988); **B327** 49 (1989); **B335** 260 (1990).

[3] A. Sansoni (CDF Collaboration), to be published in "Proceedings of the 25th Rencontres de Moriond", 17-24 March 1991, Les Arcs, France (1991).

[4] F. Paige and S. Protopopescu, BNL-38034 (1986); and in Proceedings of the 1986 Summer Study on the Physics of the Superconducting Supercollider, Donaldson, R. and Marx, J. ed, 320 (1986).

[5] C. Peterson, D. Schlatter, I. Schmitt and P. M. Zerwas, Phys. Rev. **D27** 105 (1983).

[6] S. Catani, M. Ciafaloni and F. Hautmann, Phys. Lett. **B242** 97 (1990).

[7] E. Levin, DESY Preprint DES-91-054 (1991).

[8] J. C. Collins and R.K. Ellis, Fermilab Preprint Fermilab-PUB-91/22-T (1991).

[9] N. Glover *et al.*, Z. Phys. **C38**, 473 (1988).

[10] Argus Collaboration, presented at the Conference on Physics in Collision, Durham, NC, USA (1991).

[11] M. Artuso *et al.*, (CLEO Collaboration), Phys. Rev. Lett. **62** 2233 (1989).

[12] H. Albrecht *et al.*, (ARGUS Collaboration), Phys. Lett. **B192**, 245 (1987).

[13] F. Abe *et al.*, (CDF Collaboration), Fermilab PUB-91/201-E (submitted to Phys. Rev. Lett.).

[14] F. Abe *et al.*, (CDF Collaboration), Phys. Rev. **D44** 29 (1991).

[15] C. Albajar *et al.*, (UA1 Collaboration), Phys. Lett. **B253**, 503 (1991); Trival Pal, (UA2 Collaboration) presented at the meeting of the APS Division of Particles and Fields, Vancouver, BC, Canada (1991).

[16] A.D. Martin, W.J. Stirling, and R.G. Roberts, Phys. Lett. **B228**, 149 (1989).

[17] Janet Carter, Plenary talk given at the Lepton-Photon Symposium, 25 July-1 August 1991, Geneva, Switzerland.

[18] S. D. Drell and T. M. Yan, Phys. Rev. Lett. **25** 316 (1970); S. D. Drell and T. M. Yan, Ann. Phys. **66** 578 (1971).

[19] F. Abe *et al.*, Fermilab PUB-91/169-E (submitted to Phys. Rev. Lett.).

[20] G. G. Ross, *Grand Unified Theories* (Cambridge U.P., Cambridge, 1987) and references therein. R. N. Mohapatra, *Unification and Supersymmetry* (Springer, New York, 1986). M. B. Green, J. H. Schwarz and E. Witten, eds., *Superstring Theory* (Cambridge U.P., Cambridge, 1987). R. W. Robinett and J. L. Rosner, (SO(10) models), Phys. Rev. **D25**, 3036. D. London and J. L. Rosner, (E_6 models), Phys. Rev. **D34**, 1530 (1984). J. L. Hewett and T. G. Rizzo, (review of E_6 models), Phys. Rep. **183**, 193 (1989). R. Foot, O. F. Hernandez and T. G. Rizzo, ($SU(5)_c$ models), Phys. Rev. **D41**, 2293 (1990). S. L. Glashow and U. Sarid, (two Z models), Phys. Lett. **B246**, 188 (1990). X. G. He, G. C. Joshi, H. Lew, and R. R. Volkas, (New Z' phenomenology) Phys. Rev. **D43**, R22 (1991).

[21] F. Abe *et al.*, (CDF Collaboration), Fermilab PUB-91/231-E (submitted to Phys. Rev. Lett.).

[22] T. Liss (CDF Collaboration), presented at the meeting of the APS Division of Particles and Fields, Vancouver, BC, Canada (1991).

[23] S. Kuhlmann (CDF Collaboration), presented at the Second International Symposium on Particles, Strings and Cosmology, Northeastern University, Boston, Massachusetts, USA, March 25-30 (1991).

[24] H. Baer *et al.*, Phys Lett. **B161** 175 (1985); G. Gamberini, Z. Phys. **C30** 605 (1989); G. Baer, X. Tata, and J. Woodside, Phys. Rev. **63** 352 (1989).

[25] R. K. Ellis, Fermilab - Pub - 91/30-T (1991). M. Drees and X. Tata, Phys. Lett. **B252** 695 (1990).

[26] A. Laasenan (CDF Collaboration), presented at the meeting of the APS Division of Particles and Fields, Vancouver, BC, Canada (1991).

[27] P. Harriman, A. Martin, R. Roberts and W. Stirling, Rutherford Laboratory Preprint RAL-90-007 (1990).

[28] J. Morfin and W.K. Tung, Fermilab Preprint Fermilab-Pub-90/74 (1990).

[29] F. Abe *et al.*, (CDF collaboration), Phys. Rev. Lett **62**, 613 (1989).

[30] J.A. Appel *et al.*, (UA2 Collaboration) Phys. Lett. **B160** 349 (1985).

[31] G. Arnison *et al.*, (UA1 Collaboration), Phys. Lett. **B177** 244 (1986).

[32] F. Aversa *et al.*, Phys. Lett. **B210** , 225 (1988).

[33] S. Ellis, Z. Kunszt and D. Soper, Phys. Rev. Lett., **62** 2188 (1989); Phys. Rev. Lett. **64** 2121 (1990).

[34] J. Huth *et al.*, published in "Proceedings of the 1990 Summer Study on High Energy Physics - Research Directions for the Decade ", Snowmass, Colorado, June 25 - July 13, 1990, Ed. E. Berger; preprint Fermilab CONF-90/249-E (1990).

[35] S. Ellis, Z. Kunszt and D. Soper, Private Communication.

[36] G. Marchesini and B.R. Webber, Nucl. Phys. **B310**, 461 (1988).

[37] S. Ellis, Z. Kunszt and D. Soper, Private Communication.

[38] S. Ellis, Z. Kunszt and D. Soper, Private Communication.

[39] F. Abe *et al.*, (CDF Collaboration), Fermilab Preprint Fermilab PUB-91/181, submitted to Phys. Rev. D (1991).

[40] Z. Kunszt, E. Pietarinen, Nucl. Phys. **B164** 45 (1980); T. Gottschalk, D. Sivers, Phys. Rev. **D21** 102 (1980); F. Berends *et al.*, Phys. Lett. **118B** 124 (1981).

[41] M. Mangano and S. Parke, Phys. Rep. **200** 303 (1991).

[42] P. B. Arnold, M.H. Reno, Nucl. Phys. **B319**; P.B. Arnold and R.P. Kauffman, Nucl. Phys. **B349**, 381 (1991).

[43] F. Abe *et al.*, (CDF Collaboration), Phys. Rev. Lett. **66** 2951 (1991).

[44] F. Abe *et al.*, (CDF Collaboration), FERMILAB-PUB-91/199-E, submitted to Phys. Rev. Lett. (1991).

[45] P. Aurenche *et al.*, Phys. Rev. **D42**, 1440 (1990).

[46] E. Berger, presented at the meeting of the APS Division of Particles and Fields, Vancouver, BC, Canada (1991).

[47] H. Baer, J. Ohnemus, and J.F. Owend, Phys. Lett. **B234**, 127 (1990).

[48] D. Bernard *et al.*, (UA4 Collaboration), Phys. Lett. **B198** 583 (1987).

[49] S. Shukla, (E710 Collaboration) Proceedings of the 4th International Conference on Elastic and Diffractive Scattering La Biodola, Elbe, Italy, 22-25 May 1991, to be Published in Nucl. Phys. **B** (1991).

[50] S. White, (CDF Collaboration) Proceedings of the 4th International Conference on Elastic and Diffractive Scattering La Biodola, Elbe, Italy, 22-25 May 1991, to be Published in Nucl. Phys. **B** (1991).

[51] M. M. Block, and R.N. Cahn, Phys. Lett. **B188**, 143 (1987).

[52] P. Aurenche *et al.*, Phys. Rev. **D39** 3275 (1989).

[53] F. Abe *et al.*, (CDF Collaboration), Phys. Rev. **D43**, 2070 (1991).